Combining Radar Attenuation and Partial Beam Blockage Corrections for Improved Quantitative Application

YABIN GOU[a] AND HAONAN CHEN[b,c]

[a] Hangzhou Meteorological Bureau, Hangzhou, China
[b] Colorado State University, Fort Collins, Colorado
[c] NOAA/Physical Sciences Laboratory, Boulder, Colorado

(Manuscript received 18 May 2020, in final form 25 October 2020)

ABSTRACT: Partial beam blockage (PBB) correction is an indispensable step in weather radar data quality control and subsequent quantitative applications, such as precipitation estimation, especially in urban and/or complex terrain environments. This paper developed a novel PBB correction procedure based on the improved ZPHI method for attenuation correction and regional specific differential propagation phase (K_{DP})–reflectivity (Z_H) relationship derived from in situ raindrop size distribution (DSD) measurements. The practical performance of this PBB correction technique was evaluated through comparing the spatial continuity of reflectivity measurements, the consistency between radar-measured and DSD-derived K_{DP} and Z_H relationships, as well as rainfall estimates based on $R(Z_H)$ and $R(K_{DP})$. The results showed that through incorporating attenuation and PBB corrections (i) the spatial continuity of Z_H measurements can effectively be enhanced; (ii) the distribution of radar-measured K_{DP} versus Z_H is more consistent with the DSD-derived K_{DP} versus Z_H; (iii) the measured Z_H from a C-band radar in the PBB-affected area becomes more consistent with collocated S-band measurements, particularly in the rainstorm center area where Z_H is larger than 30 dBZ; and (iv) rainfall estimates based on $R(Z_H)$ in the PBB-affected area are incrementally improved with better spatial continuity and the performance tends to be more comparable with $R(K_{DP})$.

KEYWORDS: Precipitation; Rainfall; Algorithms; Radars/Radar observations; Remote sensing

1. Introduction

Radar quantitative precipitation estimation (QPE) is critical for extreme rainfall monitoring, forecast, and decision-making during contingent flash floods, mudslides, and debris flows. However, weather radars often suffer from complete or partial beam blockage (PBB) induced by surrounding terrains (Giangrande and Ryzhkov 2005; Zhang et al. 2013; Chen et al. 2020). The PBB effect is more evident in mountainous areas and/or complex urban environments because of the blockages from mountains and buildings. As a result, the measurements of radar reflectivity Z_H behind the blocking terrain are often biased (lower than they should be), and PBB correction is necessary to fully resolve the precipitation patterns.

PBB correction methodologies based on polarimetric radar measurements have become increasingly popular in recent years (e.g., Carey et al. 2000; Giangrande and Ryzhkov, 2005; Lang et al. 2009; Zhang et al. 2013). The basis of these PBB correction schemes can be attributed to the relatively insensitive characteristics of the differential propagation phase Φ_{DP} or the specific differential propagation phase K_{DP} to PBB. In particular, the method of Carey et al. (2000) corrected the Z_H bias caused by PBB through analyzing the empirical relationship between Z_H and K_{DP} in a specific K_{DP} range, i.e., $K_{DP} \geq 1° \mathrm{km}^{-1}$ and $K_{DP} \leq 2° \mathrm{km}^{-1}$ for S-band radars. However, this method is not flexible for practical applications and cannot be applied for high-frequency radars, which suffer more from attenuation, wet radome, and miscalibration effects than S-band radars. Giangrande and Ryzhkov (2005) utilized the linear self-consistency equation between Z_H, differential reflectivity Z_{DR}, and K_{DP} in their PBB correction procedure. The linear relationship was obtained using the statistics of large samples of raindrop size distribution (DSD) measurements. The Z_H bias was derived through minimizing the area–time integrals of the radar-measured K_{DP} and the K_{DP} estimated from Z_H and Z_{DR}. However, this method requires high-quality Z_{DR} and the linear equation was only valid in pure rain situations (Giangrande and Ryzhkov 2005). The hydrometeor identification scheme, which can be used to ensure the appropriate hydrometeors are considered in the PBB correction procedure (Lang et al. 2009), also requires unbiased Z_H and Z_{DR} measurements. Zhang et al. (2013) took into account the total span of the differential phase Φ_{DP} along the radar beams in unblocked regions to dynamically estimate the Z_H bias within the blocked sectors. This method is essentially based on the nonlinear self-consistency between K_{DP}, Z_H, and Z_{DR}, which requires that Z_H and Z_{DR} are well calibrated and not affected by attenuation. This method also assumes that the precipitation characteristics in the blocked sector are similar to those in the unblocked sectors. In practical applications, the requirement of high-quality Z_H and Z_{DR} is hard to achieve, especially at higher frequencies such as C and X bands, since the attenuations caused by propagation in rain cannot be neglected. Even at S band, the attenuation can be serious during heavy rainfall events. In fact, the specific attenuation A_H is often used to quantify rainfall intensity for S-band radars (e.g., Ryzhkov et al. 2014). As such, it is challenging to extend previous PBB correction techniques designed for S-band radars to

Corresponding author: Dr. Haonan Chen, haonan.chen@colostate.edu

DOI: 10.1175/JHM-D-20-0121.1

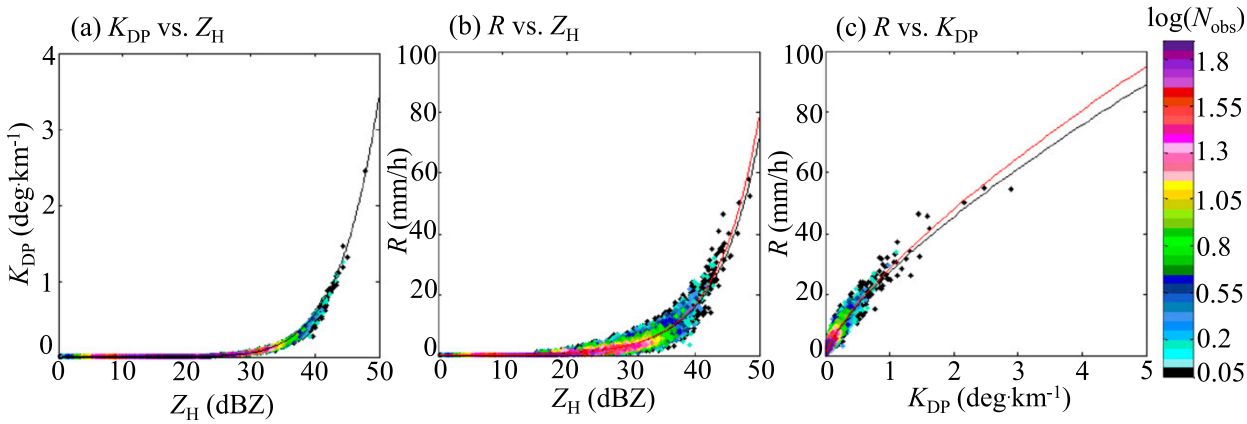

FIG. 1. Scattergrams between variables simulated from the DSD measurements between 0000 UTC 25 May 2019 and 2359 UTC 22 Jun 2019: (a) K_{DP} vs Z_H, (b) R vs Z_H, (c) R vs K_{DP}. The black curve in (a) refers to Eq. (2a); the black and red curves in (b) refer to Eqs. (5a) and (5c), respectively; and the black and red curves in (c) refer to Eqs. (5b) and (5d) in the main text, respectively.

generic applications. Although Diederich et al. (2015) utilized the Z_H–A_H relationship to estimate the Z_H bias for X-band radars, this approach is sensitive to the DSD variability and temperature, which may change dramatically along the ascending altitudes of radar beams.

In this paper, a new PBB correction procedure was developed through incorporating attenuation correction. In addition, a nonlinear K_{DP}–Z_H relationship fitted based on the local DSD measurements was incorporated into the PBB correction scheme in order to dynamically estimate the Z_H bias caused by PBB. The practical performance of this PBB correction approach was investigated using measurements from a C-band polarimetric (CPOL) radar in Hangzhou, China, during two severe rainfall events. The remainder of this paper is organized as follows: section 2 details the attenuation and PBB correction techniques; section 3 presents the demonstration study domain and dataset; section 4 addresses the practical performance of the proposed PBB correction procedure; the main findings are summarized in section 5.

2. Methodology

a. Attenuation and PBB corrections

In this study, an improved ZPHI method was adopted for attenuation correction before subsequent PBB correction. Compared to the conventional ZPHI method (Testud et al. 2000; Bringi et al. 2001), the improved attenuation correction scheme incorporates three additional constraints, including a nonnegative constraint on the A_H estimate, a constraint on the correlation coefficient ρ_{HV} in the range gate partitioning, and a stricter convergence constraint in the computational process. The main processing chain for the attenuation correction of Z_H is given as follows [for details, the readers are referred to Gou et al. (2019)]:

$$A_H(r) = \frac{[Z_H^M]^b[10^{0.1b\alpha\Delta\Phi(r_0,r_m)} - 1]}{I(r_0,r_m) + [10^{0.1b\alpha\Delta\Phi(r_0,r_m)} - 1]I(r,r_m)}, \tag{1a}$$

$$\Delta\Phi_{DP}(r_0,r_m) = \Phi_{DP}^{filtered}(r_m) - \Phi_{DP}^{filtered}(r_0), \tag{1b}$$

$$I(r_0,r_m) = 0.46b\int_{r_0}^{r_m}[Z_H^M(r)^b\,dr], \tag{1c}$$

$$I(r,r_m) = 0.46b\int_{r}^{r_m}[Z_H^M(r)^b]\,dr, \tag{1d}$$

$$\Phi_{DP}^{rec}(r_0,r_m) = \int_{r_0}^{r_m}\frac{A_H(s,\alpha)}{\alpha}ds, \tag{1e}$$

$$Z_H^{AC}(r) = Z_H^M(r) + \text{PIA}(0,r) = Z_H^M(r) + 2\int_0^r A_H(s,\alpha_{opt})\,ds, \tag{1f}$$

where Z_H^M stands for the measured reflectivity; Z_H^{AC} represents the Z_H measurements after attenuation correction; the coefficient b is set as a constant of 0.78 at C band; r refers to the range gate along a radial profile; r_0 and r_m refer to the starting and ending gates of a range segmentation, respectively; PIA(0, r) is the path integrated attenuation (PIA); $\Phi_{DP}^{filtered}$ represents the Φ_{DP} profile after filtering out the backscattering phase (i.e., δ bumps) from the measured total differential phase Ψ_{DP}; Φ_{DP}^{rec} is the reconstructed Φ_{DP} profile in the processing chain. The optimal coefficient α is searched from the predefined range [0.03, 0.18] with a step of 0.01 to minimize the difference between $\Phi_{DP}^{filtered}$ and Φ_{DP}^{rec}.

Considering the insensitivity of K_{DP} to the PBB effect, the nonlinear self-consistency relationship between K_{DP} and Z_H is utilized to estimate the optimal Z_H^B bias along each partially blocked beam through the following PBB processing chain:

$$\hat{K}_{DP} = 0.1926\times10^{-14}Z_H^{8.3965}, \tag{2a}$$

$$\Delta K_{DP} = \int_{r_b}^{r}[\hat{K}_{DP} - K_{DP}^M]\,dr, \tag{2b}$$

$$Z_H^{ABC}(r) = Z_H^{AC}(r) + Z_H^B(r), \tag{2c}$$

where the relationship between Z_H and K_{DP} is derived from simulations based on local DSD measurements (see Fig. 1a);

r_b stands for the first partially blocked range gate; Z_H^B stands for the Z_H bias caused by PBB, and it is assumed that the range gates with the same PBB ratio have the same Z_H^B bias; $\hat{K}_{DP}$ and K_{DP}^M denote the K_{DP} estimated by Z_H^{ABC} through Eq. (2a) and the K_{DP} directly estimated from $\Phi_{DP}^{filtered}$, respectively; and Z_H^{ABC} stands for the reflectivity after attenuation and PBB correction. The estimation of K_{DP} from $\Phi_{DP}^{filtered}$ is further explained in section 2b.

Through adjusting Z_H^B and iteratively imposing Z_H^B on the partially blocked range gates based on Eq. (2c), $\hat{K}_{DP}$ in Eq. (2a) can be estimated and the optimal Z_H^B can be obtained by minimizing ΔK_{DP} in Eq. (2b). Note that in practical implementations, only the range gates with $\rho_{HV} \geq 0.98$ and $\rho_{HV} \leq 1$ are taken into account in minimizing ΔK_{DP}. In addition, Z_H^B starts from 0 dBZ with an incremental step of 0.1 dBZ.

Here, it should be noted that the PBB-affected regions need to be identified before correction. Assuming that the radar-transmitted power is concentrated in the main lobe of the radar antenna pattern, one can compute the height of the radar beam center at a distance r from the radar using a general geometric optics approach, as expressed in Eq. (3):

$$H(r) = \sqrt{r^2 + (k_e R)^2 + 2rk_e R \sin\theta} - k_e R + H_0, \qquad (3a)$$

$$k_e = \left[1 + R\left(\frac{dN}{dh}\right)\right]^{-1}, \qquad (3b)$$

where R is Earth's radius; k_e is the ratio between R and the equivalent Earth's radius; dN/dh is the refractive index gradient of the standard atmosphere; θ is the antenna scan elevation angle; and H_0 is the antenna height.

The interception function between the radar beam center and the terrain elevation can be rewritten as

$$\mathrm{PBB} = (\pi a)^{-1} y\sqrt{a^2 - y^2} + a^2 \arcsin\frac{y}{a}, \qquad (4)$$

where a represents the radius of the radar beam cross section and y is the difference between the radar beam center and the terrain elevation [for more details, see Bech et al. (2003)]. Accordingly, the PBB ratios at different range gates and azimuthal angles can be derived, and the PBB correction is executed upon the partially blocked range gates.

b. Processing of Z_H, Ψ_{DP}, and K_{DP}

The terms Z_H, Φ_{DP}, and K_{DP} are three key radar variables utilized in the data processing described in section 2a. In this study, several quality control steps were implemented to ensure the creditability of these measurements. In particular, in order to eliminate ground clutter contaminations, the clutter mitigation decision (CMD) algorithm described in Hubbert et al. (2009) was adopted to identify and suppress ground clutter from the radar signals. The CMD algorithm incorporates clutter phase alignment from I (in phase) and Q (quadrature phase), the spatial texture and spin change of Z_H, the standard deviations of Z_{DR} and Ψ_{DP}, and a fuzzy logic scheme (see also Hubbert et al. 2009).

In Ψ_{DP} processing, a nine-gate smoothing is first utilized to suppress and remove spike signals with large fluctuations within a short range along a radial profile. A Ψ_{DP} dealiasing procedure is then executed based on the standard deviation of Ψ_{DP} derived from the nine aligned range gates (Wang and Chandrasekar 2009). Then, the iterative filtering method (Hubbert and Bringi 1995) is applied to filter the potential backscatter differential phase along the Ψ_{DP} profile. Consequently, a high-quality Φ_{DP} profile can be derived after subtracting the initial system phase of Ψ_{DP}.

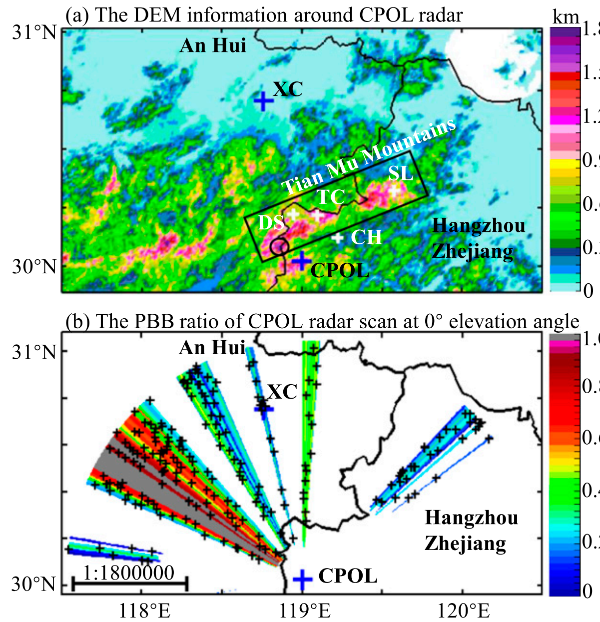

FIG. 2. (a) The digital elevation model (DEM) information around the CPOL radar; (b) the partial beam blockage (PBB) ratio of 0° elevation scan of the CPOL radar. The four white "+" in (a) indicate the locations of the four disdrometer units, the black "+" in (b) indicates the gauge network in the partially blocked areas, and the blue "+" indicates the location of the Xuan Cheng (XC) S-band and CPOL radars. The PBB ratio in (b) was derived using the refraction index under the standard atmospheric conditions.

The K_{DP} is estimated along the Φ_{DP} range profile using the linear fitting approach detailed by Wang and Chandrasekar (2009), with an additional nonnegative constraint on the K_{DP} estimates, as well as a monotonic increasing constraint on the reconstructed Φ_{DP} in the fitting process. In addition, if there is no range gate featuring $\rho_{HV} > 0.85$ in the nine consecutive gates, these gates are removed to avoid possible contamination from nonuniform beam filling (NUBF). The additional constraints on the K_{DP} estimation aim to ensure the high quality of K_{DP} for PBB correction and K_{DP}-based radar rainfall retrievals.

c. Radar QPE estimators and evaluation metrics

Utilizing four Parsivel (particle size and velocity) disdrometer units deployed in the northwest of Hangzhou (see Fig. 2a), we collected a large amount of in situ DSD data under the radar coverage domain (detailed in section 3). However, instead of deriving "fixed" climate radar rainfall estimation algorithms for local applications using the DSD data collected during a large number of precipitation events, this study used the 6371 DSD samples collected from 25 to 27 May 2019 and 15 017 DSD samples collected from 17 to 20 June 2019 to derive the radar rainfall relationships particularly suitable for these two precipitation events. The main goal was to quantify the impact of PBB correction on the radar QPE performance during these two selected events: event 1 (25–27 May 2019) was dominated by large-scale moderate rain, whereas event 2 (17–20 June 2019) was dominated by torrential heavy rain. A more detailed description of these two precipitation events is provided in section 3b.

The radar rainfall relationships for these two events are established as

$$R(Z_H) = \begin{cases} 0.0529 \times Z_H^{0.6196}, & Z_H < 40\,\mathrm{dB}Z \\ 0.0968 \times Z_H^{0.5764}, & Z_H \geq 40\,\mathrm{dB}Z \end{cases}, \tag{5a}$$

$$R(K_{\mathrm{DP}}) = 23.3894 \times K_{\mathrm{DP}}^{0.7491}, \tag{5b}$$

$$R(Z_H) = \begin{cases} 0.0689 \times Z_H^{0.6197}, & Z_H < 40\,\mathrm{dB}Z \\ 0.1054 \times Z_H^{0.5859}, & Z_H \geq 40\,\mathrm{dB}Z \end{cases}, \tag{5c}$$

$$R(K_{\mathrm{DP}}) = 28.5717 \times K_{\mathrm{DP}}^{0.7472}, \tag{5d}$$

where Eqs. (5a) and (5b) are for event 1 and Eqs. (5c) and (5d) are for event 2. Equations (5a)–(5d) were fitted using the standard weighted least squares method based on the simulated Z_H and K_{DP} and the rain rates R computed directly from the DSD data (see Figs. 1b,c). The polarimetric radar observables were simulated at C-band frequency using the T-matrix method (Waterman 1965). Therein, the raindrop aspect ratio of Brandes et al. (2002) was adopted, and the temperature was obtained from a local sounding station. In Eqs. (5a) and (5c), two Z–R relationships were utilized to discriminate light–moderate rain ($Z_H < 40\,\mathrm{dB}Z$) from moderate–heavy rain ($Z_H \geq 40\,\mathrm{dB}Z$). The differences between Eqs. (5a) and (5b) and Eqs. (5c) and (5d) also reflect that different precipitation microphysical characteristics were observed in the two events. With such event-based rainfall algorithms, the uncertainties inherent in radar rainfall relationships can be reduced so as to further highlight the impact of attenuation and PBB corrections.

Radar hourly rainfall accumulations based on $R(Z_H)$ and $R(K_{\mathrm{DP}})$ were then derived using the pixel-to-pixel linear average accumulation scheme as follows:

$$R_{\mathrm{hour}} = \frac{(t_1 - t_{\mathrm{st}})}{t_{\mathrm{total}}} \times \frac{(R_0 + R_1)}{2} + \sum_{i=1}^{n-2} \frac{(t_{i+1} - t_i)}{t_{\mathrm{total}}} \times \frac{(R_i + R_{i+1})}{2} + \frac{(t_{\mathrm{ed}} - t_{n-1})}{t_{\mathrm{total}}} \times \frac{(R_{n-1} + R_n)}{2}, \tag{6}$$

where R_{hour} refers to the hourly rainfall estimates accumulated through the time series of R_i obtained in different time frames; the average of R_i and R_{i+1} is used to represent the rainfall intensity during the time window from t_i and t_{i+1}; t_{st} and t_{ed} refer to the starting and ending time of the time series; t_{total} is the difference between t_{ed} and t_{st} (i.e., 1 h in this study); t_i and t_{i+1} refer to the starting or ending time of R_i and R_{i+1}, and their difference ranges from 170 to 230 s for the CPOL radar.

The 3-h rainfall estimates were then derived by aggregating the hourly rainfall estimates R_{hour}, which were then used in the verification analysis mainly because the longer-term temporal averaging could further reduce the random errors involved in the radar measurements. The radar QPE performance was quantitatively evaluated through comparison with corresponding gauge rainfall measurements. In particular, the performance of different radar rainfall estimators within the PBB area was investigated. Four evaluation scores, including the mean bias E_{BIAS}, the normalized mean absolute error E_{NM}, the root-mean-square error E_{RMS}, and the correlation coefficient E_{CC}, were used to quantify the impact of PBB correction on the rainfall estimation:

$$E_{\mathrm{BIAS}} = \frac{\sum_{i=1}^{n} r_i}{\sum_{i=1}^{n} g_i}, \tag{7a}$$

$$E_{\mathrm{NM}} = \frac{\sum_{i=1}^{n} |r_i - g_i|}{\sum_{i=1}^{n} g_i} \times 100\%, \tag{7b}$$

$$E_{\mathrm{RMS}} = \sqrt{\frac{1}{n}\sum_{i=1}^{n} (r_i - g_i)^2}, \tag{7c}$$

$$E_{\mathrm{CC}} = \frac{\sum_{i=1}^{n} (r_i - \overline{r})(g_i - \overline{g})}{\sqrt{\sum_{i=1}^{n} (r_i - \overline{r})^2}\sqrt{\sum_{i=1}^{n} (g_i - \overline{g})^2}}, \tag{7d}$$

where n is the sample number; r_i and g_i stand for the radar-estimated and the gauge-observed 3-h rainfall accumulations, respectively; $\overline{r}$ and $\overline{g}$ stand for their average values, respectively.

3. Demonstration study domain and dataset

As shown in Fig. 2a, the study domain is mainly located to the north and northwest of the CPOL radar deployed in the south Tian Mu Mountains (TMM) over eastern China. The coverage of the CPOL radar shown in Fig. 2b is 150 km. Most of this area (the rectangular region in Fig. 2a) is located between the provinces of Anhui and Zhejiang. Qing Liang Peak (QLP) is the highest peak (1787.4 m above mean sea level, the circle in Fig. 2a) to the west of Zhejiang Province. Due to the complex mountainous terrain and the orographic enhancement of precipitation, this domain often suffers from severe rainfall that causes catastrophic flooding. Strong precipitation systems are frequently triggered when the western air flows with abundant moisture pass through this area during the summer monsoon seasons.

a. Radar and surface observations

Considering the high altitude of the CPOL radar (1512 m above mean sea level), we reconfigured its volume coverage pattern (VCP) mode from March 2018 to enhance its capability to monitor rapidly developing severe rainstorms. The current

VCP scan mode includes 11 elevation angles: 0°, 0.5°, 1.5°, 0°, 2.5°, 3.5°, 4.5°, 6.0°, 7.5°, 9.0°, and 12°. The azimuthal resolution was set as 0.5° at the lowest five elevation angles and 0.98° at the other six elevations. The scan strategy was rigorously implemented to complete one VCP scan in 6 min. Note that the lowest elevation angle (i.e., 0°) was repeated twice within a VCP scan cycle in order to improve the temporal resolution so as to capture more low-level details of fast-evolving rainstorms. We also want to note that the CPOL radar is the first and only radar site that adopts such flexible VCP in China, which is groundbreaking from an operational perspective.

However, the 0° elevation angle of the CPOL radar is completely blocked in the azimuth directions of [298.5°, 308°] (see Fig. 2b) due to the QLP, which is located only 17 km from the CPOL radar. In addition, some azimuths in the north and northwest directions of the CPOL radar are partially blocked, as indicated in Fig. 2b.

The gauge network within the PBB-affected area of the CPOL radar includes 219 tipping-bucket gauge stations, and their sampling resolution is 1 min. All of the gauges are well maintained by the local meteorological bureaus, and they are considered one of the most important data sources for severe rainfall monitoring and warnings. The gauge measurements were aggregated and only rainfall time series without any transmission interruptions were used in this study.

In addition, four Parsivel disdrometer units were deployed in the north mountainous areas of Hangzhou (see white "+" in Fig. 2a), including the Dao Shi (DS), Tian Chi (TC), Changhua (CH), and Shi Ling (SL) stations. The disdrometers were used to collect in situ DSD data in the study domain, and the temporal resolution of these disdrometers was configured as 1 min. All of these disdrometer stations are equipped with municipal electricity and an optical fiber, and they are well maintained to ensure the quality of the measured DSD. As mentioned in section 2c, 21 388 one-minute DSD samples were used to derive the appropriate K_{DP}–Z_H relationship and the radar rainfall estimators.

b. Brief overview of the selected precipitation events

As mentioned, two convective rainstorm events during the monsoon season in 2019 were investigated in this paper. The rainfall during the first event (25 May 2019) was characterized by continuous rainfall over 12 h, with some hourly accumulations exceeding 20 mm. The widespread rainstorms slowly passed over the target domain from the southwest to the northeast between 0600 and 2000 UTC 25 May 2019. During this event, the maximum 12-h rainfall accumulation recorded by gauges reached 187.3 mm in Shuang County of Xuan Cheng (XC) city at 2200 UTC 25 May 2019, and the rainfall measurements at more than 10 gauge stations in Huangshan city exceeded 100 mm during this 12-h period. The other event was a severe convective rainfall event that occurred on 20 June 2019. Large amounts of rainfall were recorded in most areas of XC city between 1800 and 2100 UTC 20 June 2019. The 3-h rainfall accumulation at the Seven Tower station reached 105.2 mm, and many villages suffered serious flooding and waterlogging.

The Z_H measurements from the 0° elevation scans were seriously degraded. As indicated by the plan position indicator (PPI) plots in Figs. 3a and 3b, the Z_H patterns exhibit obvious discontinuity along the west and north azimuthal directions of the CPOL radar. This discontinuity corresponds to the radar beams that suffer from PBB due to the TMM. In addition, the maximum Φ_{DP} values in the azimuthal directions pointing to XC city were increased over 100° (see Figs. 3c,d), which implies that significant attenuation might be involved in the CPOL radar measurements in both the PBB and non-PBB areas. In contrast to the Z_H measurements in Figs. 3a and 3b, the K_{DP} in Figs. 3e and 3f present good continuity without being affected by attenuation or PBB. Again, in this case, it is difficult to use conventional approaches to simultaneously correct the Z_H biases caused by attenuation and PBB.

4. Results and discussion

The practical performance of the designed PBB correction scheme was verified through comparing the CPOL radar reflectivity with the collocated S-band reflectivity measurements from the XC radar and the reflectivity simulated from the DSD data. The impact of PBB correction on radar QPE was thoroughly investigated by comparing the continuity of the radar rainfall field derived from uncorrected and corrected Z_H. Cross comparisons with gauge rainfall measurements and the rainfall estimates derived from $R(K_{DP})$ were also performed.

a. Comparison with the DSD-based simulations

Ideally, the scattergram of radar-measured K_{DP} versus Z_H should roughly follow the black curves (regression curves from the DSD data) in Figs. 4a and 4b (for the PBB-affected areas). However, a large number of scatter points deviate from the simulated curves. Most of these outliers correspond to small Z_H^M ($Z_H < 40$ dBZ) and high K_{DP} ($K_{DP} > 1°$ km^{-1}), as indicated by the ellipses. High liquid water content was anticipated for these large K_{DP} measurements, which should be characterized by higher Z_H; however, high Z_H^M was not observed because of the attenuation and PBB effects.

After attenuation correction, the scattergrams of K_{DP} versus Z_H^{AC} in Figs. 4c and 4d are more consistent with the theoretical curves compared to Figs. 4a and 4b, especially when Z_H^{AC} is larger than 40 dBZ. In addition, the spatial continuity of Z_H^{AC} in Figs. 5c and 5d is more reasonable than that in Figs. 5a and 5b. Such enhancement can be attributed to the attenuation correction on Z_H. Nevertheless, there are still many scatter points with $Z_H < 40$ dBZ and $K_{DP} > 1°$ km^{-1} (see ellipses in Figs. 4c,d), which correspond to the radial gaps in the PBB areas indicated in Figs. 5a and 5b.

After correcting the PBB, the scattergrams of K_{DP} versus Z_H^{AC} in Figs. 4e and 4f present a coherent distribution and they follow the theoretical K_{DP}–Z_H curves fairly well. At the same time, Z_H^{ABC} in Figs. 5e and 5f exhibits better spatial continuity than that in Figs. 5c and 5d, and the radial gaps have been completely eliminated. It can be concluded that the residual bias of Z_H^{AC} caused by PBB (i.e., data in the ellipses in Figs. 4c,d) were effectively corrected after the PBB correction. The overall scattergram of the radar-measured K_{DP} versus Z_H is more consistent with that simulated from DSD, demonstrating the effectiveness of the PBB correction procedure.

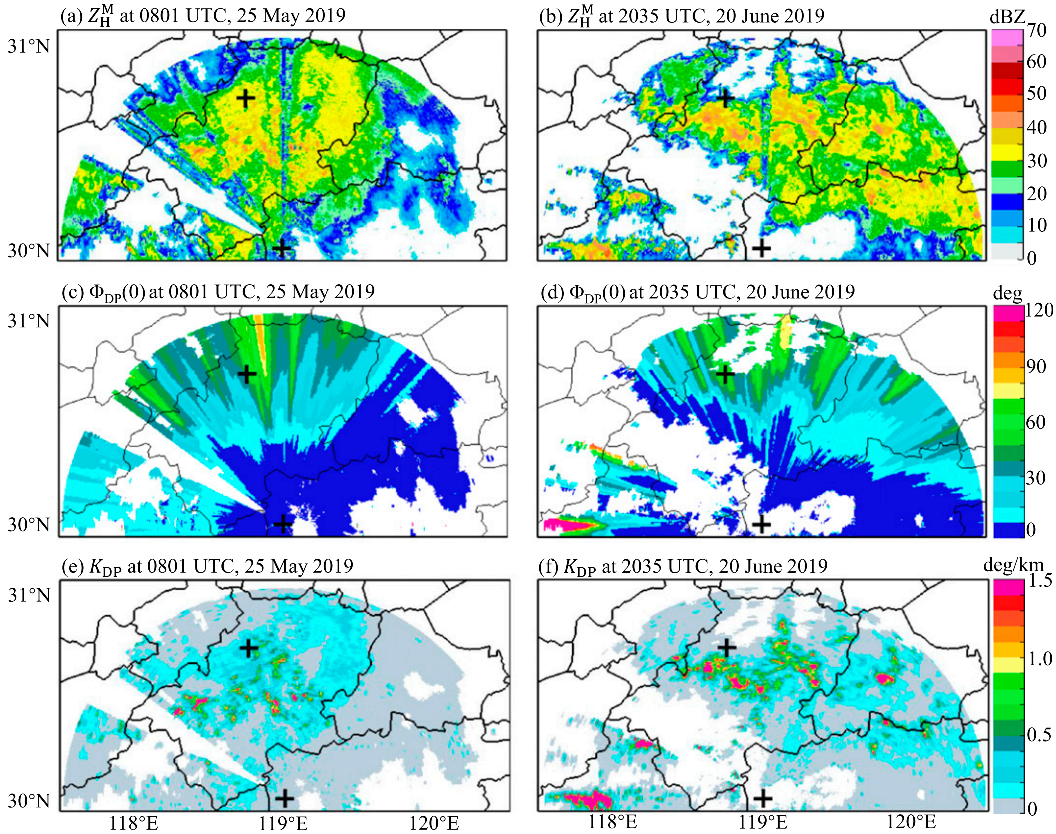

FIG. 3. Plan position indicator (PPI) observations of the CPOL radar at the 0° elevation angle: (a),(c),(e) Z_H^M, Φ_{DP}(0), and K_{DP} collected at 0801 UTC 25 May 2019; (b),(d),(f) As in (a),(c),(e), but collected at 2035 UTC 20 Jun 2019. The black "+" indicates the locations of the XC and CPOL radars.

b. Comparison with the S-band XC radar measurements

To further verify the attenuation and PBB correction performance, Z_H measurements from the CPOL radar were compared with the Z_H measurements from a nearby S-band radar, which is a well-calibrated single-polarization system. The comparison was performed in the common sampling volumes (overlapped range gates) that were not affected by PBB for both the CPOL and XC radars. To this aim, the matched Z_H measurements from the CPOL and XC radars were selected. In particular, if the altitude differences between the two radar beams in their overlapped area were less than 0.01 km, the common sampling volumes were considered available and the corresponding data pairs were selected for comparison. In total, 62 598 data pairs were selected between 0700 and 0900 UTC 25 May 2019 for event 1, and 40 138 data pairs were selected between 1930 and 2130 UTC 20 June 2019 for event 2.

The scattergrams of K_{DP} versus Z_H^M and K_{DP} versus Z_H^{AC} of the CPOL radar in the selected common sampling volumes are shown in Figs. 6a–d. As indicated in Figs. 6a and 6b, some Z_H^M measurements suffered from serious attenuation in the areas not affected by PBB and the scatter density distributions deviate far from the theoretical curves derived from the DSD data. After attenuation correction, Z_H^{AC} in the non-PBB areas were effectively enhanced, and the scattergrams of K_{DP} versus Z_H^{AC} are more coherent with the theoretical curves (see Figs. 6c,d). In addition, Z_H^{AC} in the non-PBB-affected areas can be used to cross check the quality of the Z_H measurements from the S-band XC radar. Figures 6e and 6f show the scattergram of Z_H^{AC} from the CPOL radar versus the Z_H measurements from the XC radar in the common sampling volumes. Note that an additional constraint of $K_{DP} > 0.1° \text{km}^{-1}$ was imposed in this comparison in order to alleviate the impact of weaker echoes. As a result, 28 210 and 12 576 sample pairs were included in Figs. 6e and 6f, respectively. As expected, Figs. 6e and 6f show obvious consistency between the two radar systems. Compared to the Z_H^M measurements in Figs. 5a and 5b, Z_H^{AC} in Figs. 5c and 5d in the non-PBB-affected areas presents a more consistent spatial pattern with the S-band Z_H measurements illustrated in Figs. 5g and 5h.

The arithmetic bias between the reflectivity measurements from these two radars was also computed as follows:

$$\Delta Z_H(Z_T) = \frac{1}{n}\sum[Z_H^C(Z_T) - Z_H^S(Z_T)], \tag{8}$$

where n is the total number of common sampling resolution volumes between the XC and CPOL radars; Z_H^C stands for the C-band reflectivity (i.e., Z_H^M,Z_H^{AC}, or Z_H^{ABC}); and Z_T is a reflectivity threshold used to take into account the beam-filling

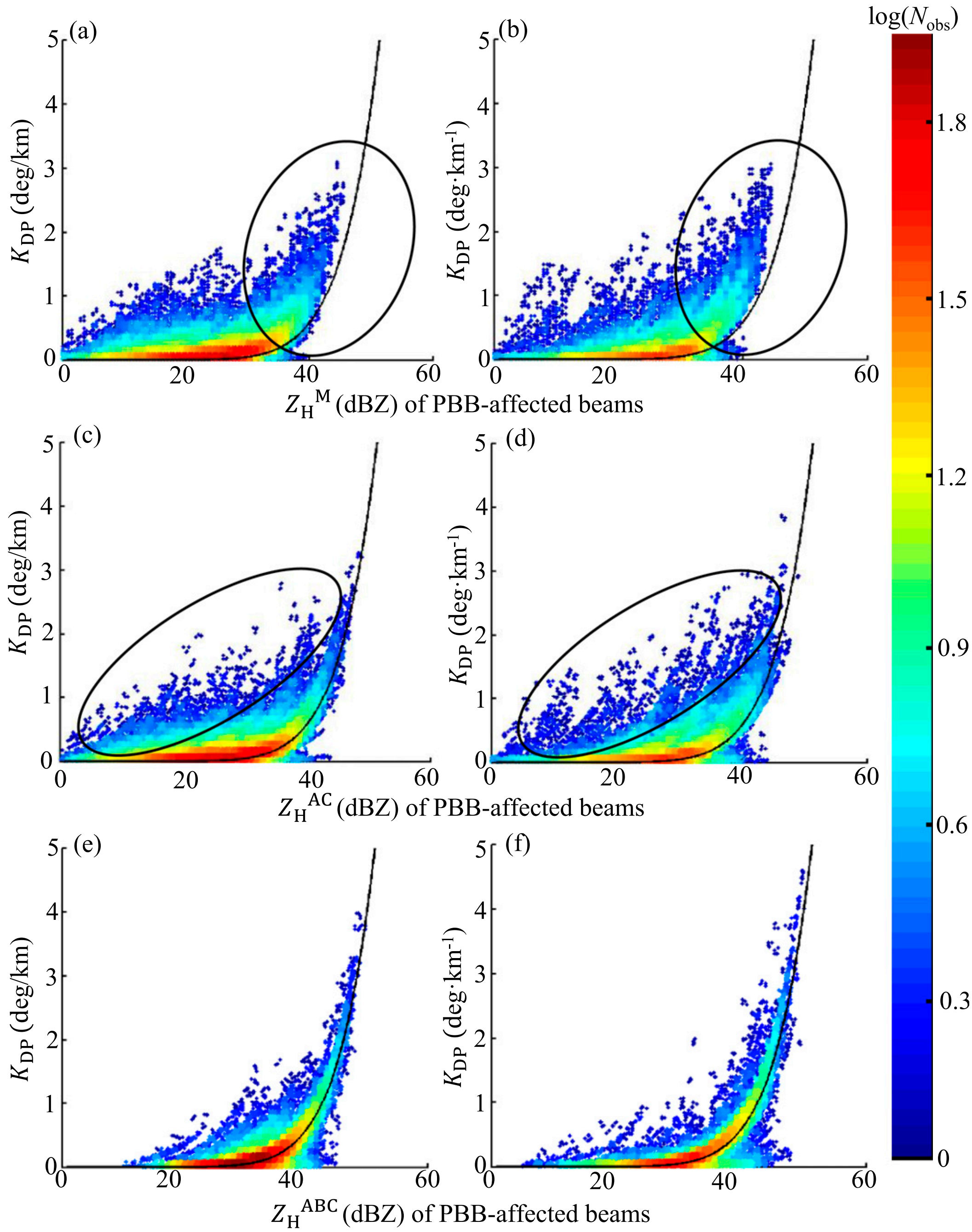

FIG. 4. The scattergram of K_{DP} vs Z_H within the PBB-affected area of the CPOL radar: (a),(b) K_{DP} vs Z_H^M shown in Figs. 3a and 3b; (c),(d) K_{DP} vs Z_H^{AC} shown in Figs. 5c and 5d; (e),(f) K_{DP} vs Z_H^{ABC} shown in Figs. 5e and 5f. The black curve in exponential form corresponds to Eq. (2a) in the main text.

issue of the XC radar, since the range and azimuthal resolutions of the XC radar (1000 m) are coarser than that of the CPOL radar (125 m). The threshold Z_T is particularly important near the edge of a rainstorm, where the precipitation echoes may completely fill the CPOL radar range volumes, but only partially fill the XC radar range volumes. Accordingly, when $Z_T > 20$ dBZ, ΔZ is 1.31 and 3.11 dBZ in Figs. 6e and 6f, respectively; when $Z_T > 30$ dBZ, ΔZ is -0.49 and 0.88 dBZ, respectively. This indicates excellent agreement between the Z_H measurements from the S-band XC radar and the CPOL radar, especially in heavy rainfall regions.

In the PBB-affected areas, the Z_H^M measurements from the CPOL radar (see Figs. 5a,b) are much lower than those from the XC radar (see Figs. 5g,h). As shown by the scattergram in

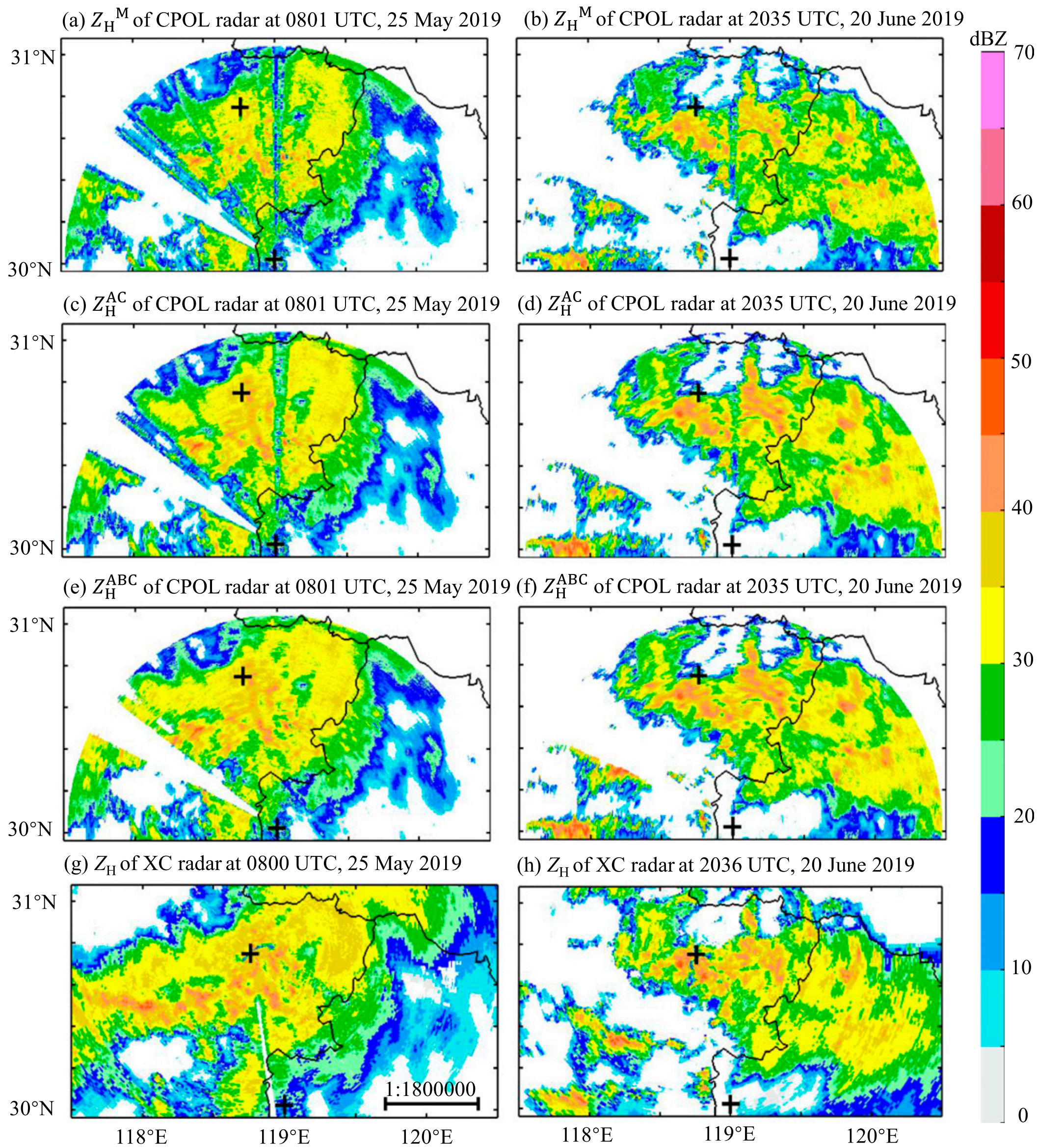

FIG. 5. PPI observations of the CPOL and S-band XC radars: (a),(b) Z_H^M measurements at the 0° elevation angle at 0801 UTC 25 May 2019 and 2035 UTC 20 Jun 2019, respectively; (c),(d) Z_H^{AC} measurements corresponding to (a) and (b); (e),(f) Z_H^{ABC} measurements corresponding to (a) and (b); (g),(h) Z_H measurements from the S-band XC radar at the 1.5° elevation angle. The black "+" marks indicate the locations of the CPOL and XC radars.

Figs. 7a and 7d, many sample pairs are distributed below the diagonal line, and ΔZ is -4.12 and -3.63 dBZ, respectively, when $Z_T > 20$ dBZ. After attenuation correction, the Z_H^{AC} measurements in the PBB-affected area were slightly enhanced, as illustrated in Figs. 5c and 5d. Nevertheless, Figs. 7b and 7e show that there are still many sample pairs that are distributed below the diagonal line, and ΔZ is -3.85 and -2.30 dBZ, respectively, when $Z_T > 20$ dBZ. This, again, indicates that the PBB effect cannot be resolved only with attenuation correction.

In contrast, Z_H^{ABC} in Figs. 5e and 5f shows more continuous reflectivity patterns with less PBB contamination. The reflectivity patterns also agree well with the XC S-band measurements in Figs. 5g and 5h. As shown in Figs. 7c and 7f, most of the data pairs are distributed along the diagonal line, similar to the measurements in the regions not affected by PBB (see Figs. 6e,f). The ΔZ in Figs. 7c and 7f is 0.64 and 2.74 dBZ, respectively, when using a threshold of $Z_T > 20$ dBZ. The larger ΔZ in event 2 is likely due to the beam-filling issues, and it can be reduced to 0.16 dBZ when using a threshold of $Z_T > 30$ dBZ.

c. *Impact on the radar QPE*

In this study, radar-derived rainfall accumulations were used as another way to demonstrate the practical performance of

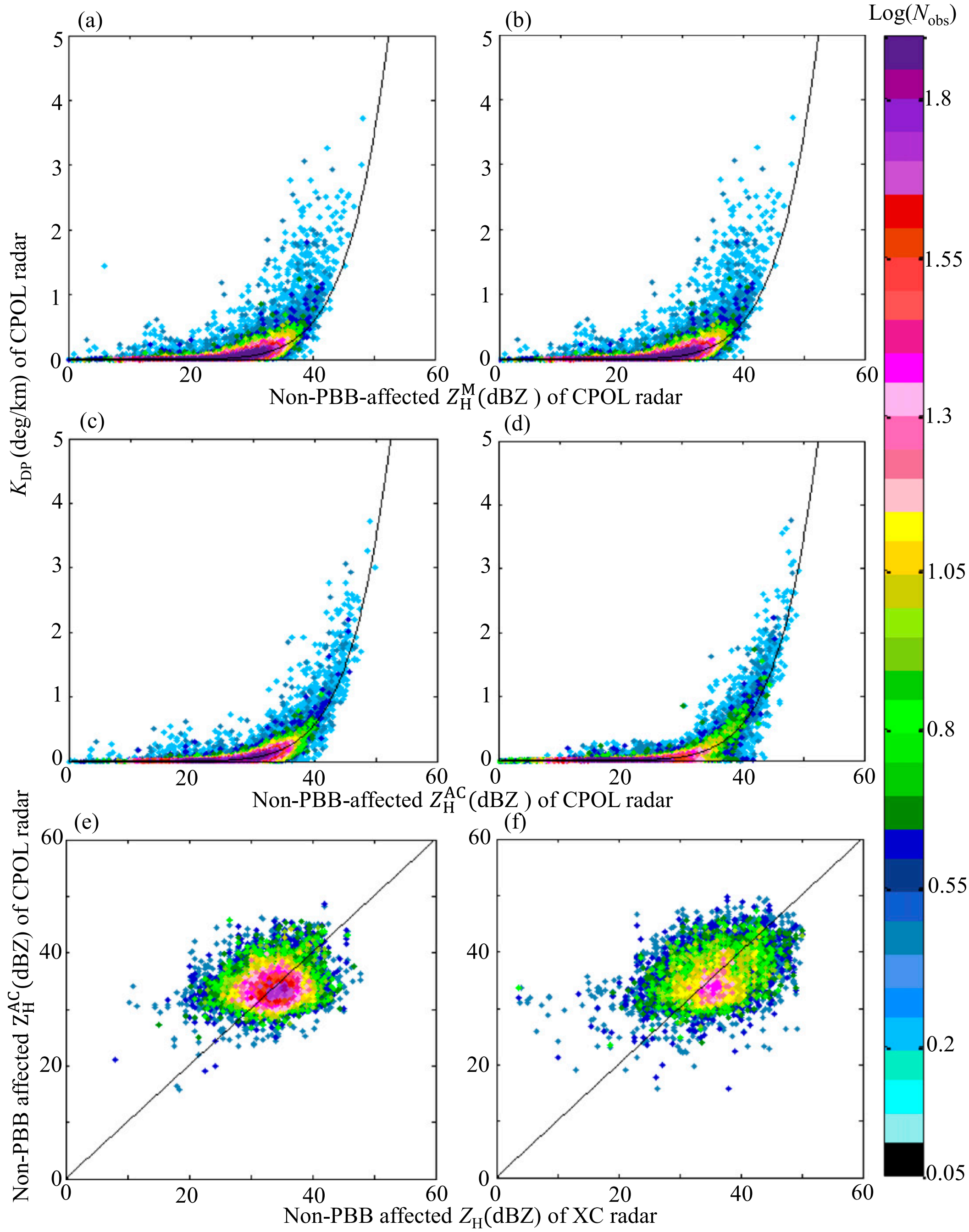

FIG. 6. Scatter density plots of (a),(b) K_{DP} vs Z_H^M and (c),(d) K_{DP} vs Z_H^{AC} of the CPOL radar for the common (overlapped) range gates between the S-band XC radar and the CPOL radar without any PBB; (e),(f) Z_H^{AC} of the CPOL radar vs Z_H of the XC radar for the common range gates. Shown are (left) event 1 and (right) event 2. The black curve in exponential form in (a)–(d) corresponds to Eq. (2a) in the main text.

the designed PBB correction procedure. Hereafter, the radar QPE estimators based on Z_H^M, Z_H^{AC}, and Z_H^{ABC} are denoted by $R(Z_H^M)$, $R(Z_H^{AC})$, and $R(Z_H^{ABC})$, respectively. The radar-derived 3-h rainfall fields were investigated, in particular, since the random errors could be eliminated through temporal averaging. The analysis was performed from the following aspects:

1) SPATIAL CONTINUITY OF THE RAINFALL FIELD

As shown by the examples in Figs. 8a–d, although $R(Z_H^{AC})$ presents enhanced and higher rainfall estimates than $R(Z_H^M)$ in the non-PBB-affected areas due to attenuation correction, the rainfall fields derived from both $R(Z_H^M)$ and $R(Z_H^{AC})$ present serious spatial discontinuity with large gaps along the PBB-affected

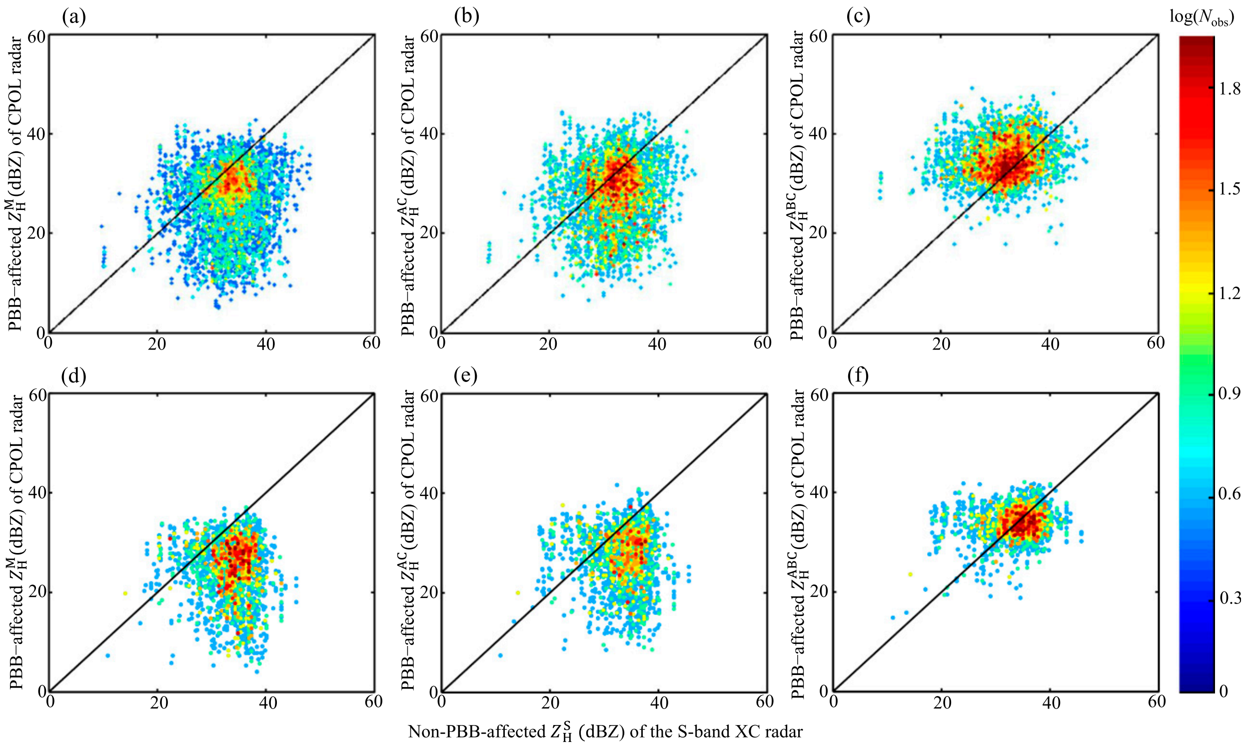

FIG. 7. Cross comparison of the measurements from the CPOL and XC radars for the common range gates: (a)–(c) PBB-affected Z_H^M, Z_H^{AC}, and Z_H^{ABC}, respectively, of the CPOL radar vs the non-PBB-affected Z_H^S of the XC radar during event 1; (d)–(f) as in (a)–(c), but for event 2. The black line indicates the 1:1 line.

radial profiles, indicating obvious underestimation of $R(Z_H^{AC})$ in this area. In contrast, the rainfall textures of $R(Z_H^{ABC})$ in Figs. 8e and 8f show better spatial continuity than those of $R(Z_H^M)$ and $R(Z_H^{AC})$. In addition, $R(Z_H^{ABC})$ is more consistent with $R(K_{DP})$ in Figs. 8g and 8h. Such improvement demonstrates that the Z_H measurements at the 0° elevation angle in all time frames were corrected properly.

According to sections 2a and 2b, an improvement in continuity can be introduced by combining attenuation and PBB corrections. The contribution of attenuation correction, the first term in Eq. (2c), depends on the PIA$(0, r_0)$ along the radial profile. It is tightly related to A_H, which is derived using the dynamic α_{opt} coefficient. As depicted in Fig. 9a, the max PIA value at the last range gate along a radial profile (azimuthal angle of 0.25°) of the 0° elevation angle scan is 2.33 dB (difference between the red and green curves). Similarly, the max PIA value is 2.18 dB at the last range gate along the radial of azimuthal angle of 0.08° (see Fig. 9b).

The second term in Eq. (2c), i.e., $Z_H^B(r_b)$, is tightly associated with the PBB ratios; it is also the main part of the proposed PBB correction procedure. However, the atmospheric states are always changing, indicating that PBB correction with fixed $Z_H^B(r_b)$ based on the blockage ratios derived at standard atmospheric conditions may not be appropriate. In this paper, $Z_H^B(r_b)$ was also dynamically determined based on the insensitivity of K_{DP} to the PBB effect. In particular, $Z_H^B(r_b)$ in Figs. 9a and 9b is 17.83 and 16.98 dBZ (i.e., difference between the blue and red curves), respectively, which are much larger than the max PIA values along the same radial directions. That is to say, the PBB correction contributes more to the spatial continuity of the radar reflectivity measurements and rainfall estimates than the attenuation correction.

2) Comparison with the gauge measurements

For the sake of comparison, the radar rainfall estimates were deemed to agree well with the gauge rainfall measurements if $|r_i - g_i| < 5$ mm. Note that both the radar and gauge rainfall measurements were of a 3-h scale. To see the clear trends of the rainfall scatters, three diagonal lines were included in the rainfall comparisons in Fig. 10, namely, the upper diagonal line ($y = x + 5$), the middle diagonal line ($y = x$), and the lower diagonal line ($y = x - 5$). According to the E_{BIAS} scores in Table 1, $R(Z_H^{AC})$ slightly reduced the underestimation of $R(Z_H^M)$ after attenuation correction. Consequently, the E_{NM}, E_{RMS}, and E_{CC} scores of $R(Z_H^{AC})$ improved by 7.7%, 17.6%, and 5.6%, respectively, for the estimates on 25 May 2019 and by 14%, 5.5%, and 7.6%, respectively, for the estimates on 20 June 2019. Nevertheless, there are no obvious differences between the scatter distributions in Figs. 10a and 10b, or Figs. 10e and 10f. More than 20% of the scatters are distributed below the lower diagonal line, which indicates that the underestimation of $R(Z_H^M)$ can hardly be resolved with attenuation correction.

In contrast, the E_{BIAS} scores of $R(Z_H^{ABC})$ are close to 1. After applying $R(Z_H^{ABC})$, nearly all of the scatters distributed below the lower diagonal line in Figs. 10b and 10f were enhanced,

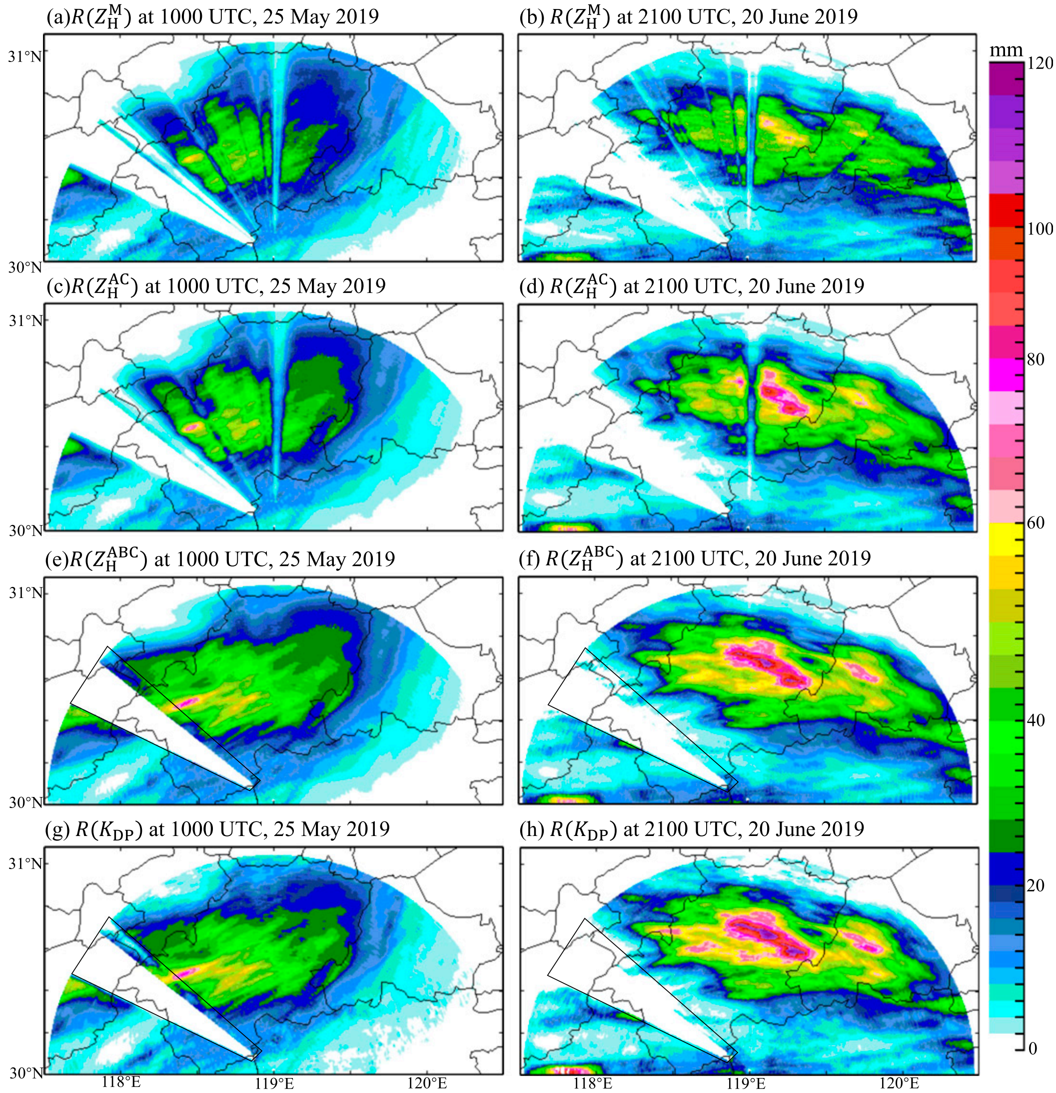

FIG. 8. Three-hour rainfall estimates based on the CPOL radar PPI observations at the 0° elevation angle: (a),(b) derived from $R(Z_H^M)$; (c),(d) derived from $R(Z_H^{AC})$; (e),(f) derived from $R(Z_H^{ABC})$; (g),(h) derived from $R(K_{DP})$. (left) Estimates at 1000 UTC 25 May 2019 and (right) estimates at 2100 UTC 20 Jun 2019.

as shown in Figs. 10c and 10g. Much fewer scatters can be found below the lower diagonal lines. We also noted that most of the underestimated values are located in the rectangles illustrated in Figs. 8e and 8f. Since radar beams are completely blocked when the PBB ratios are close to 1, the radar signals are extinct at farther range gates in this area. This is also why we still have some radial gaps in Figs. 8e and 8f in the completely blocked area. In addition, the radar estimates of $R(Z_H^{ABC})$ in Figs. 10c and 10g were overestimated at some points, conversely demonstrating the enhanced Z_H along these radials after PBB correction.

As the most important result, $R(Z_H^{ABC})$ further reduced the underestimation involved in $R(Z_H^{AC})$. The E_{NM} and E_{RMS} scores of $R(Z_H^{ABC})$ decreased by 72.7% and 67.8%, respectively, for the first event, and by 56.5% and 55.8%, respectively, for the second event. Meanwhile, the E_{CC} scores increased by 59.6% and 12.9%, respectively, for the two events. The relative improvements of $R(Z_H^{ABC})$ to $R(Z_H^{AC})$ quantitatively demonstrate the necessity and effectiveness of the PBB correction procedure.

3) COMPARISON WITH $R(K_{DP})$

The $R(K_{DP})$ can be used as another objective reference because of the insensitivity of K_{DP} to attenuation and PBB. First, the E_{BIAS} scores of $R(K_{DP})$ in Table 1 indicate that $R(K_{DP})$ slightly underestimated the rainfall. However, such underestimation mainly exists when the gauge rainfall measurements were less than 20 mm for the 25 May 2019 event, or less than 40 mm for the 20 June 2019 event (see Figs. 10d,h). Otherwise, an overestimation of $R(K_{DP})$ can be observed. As a result, nearly all of the scores of $R(K_{DP})$ listed in Table 1 are inferior to that of $R(Z_H^{ABC})$. This also indicates that the combination of different rainfall relationships can more

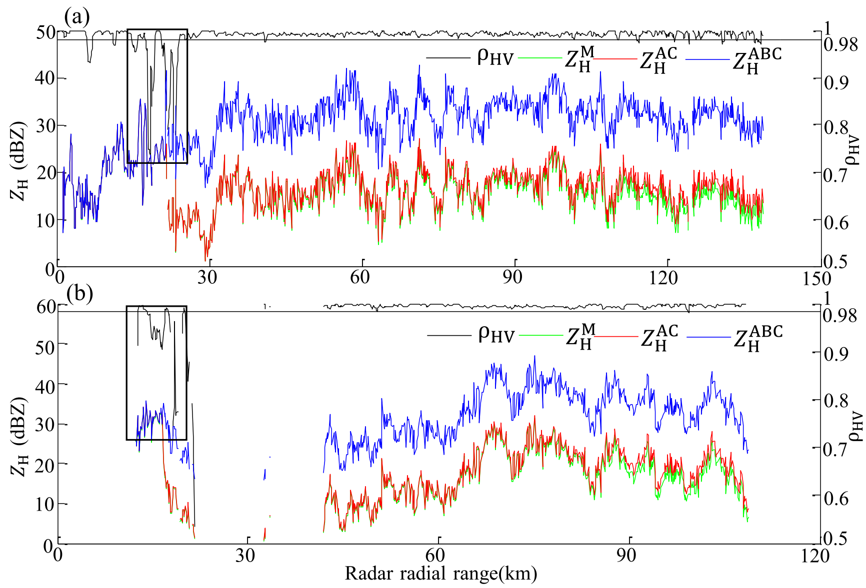

FIG. 9. Example radial range profiles of the CPOL radar at the 0° elevation angle: (a) Azimuthal angle is 0.25° at 0801 UTC 25 May 2019; (b) azimuthal angle is 0.08° at 2035 UTC 20 Jun 2019. The rectangles in (a) and (b) indicate the location of the terrain.

adequately represent the precipitation characteristics of the rainstorms.

Second, the rainfall textures of $R(Z_H^M)$ in Figs. 8a and 8b, and of $R(Z_H^{AC})$ in Figs. 8c and 8d in the PBB-affected area present many more discontinuities than that of $R(K_{DP})$ in Figs. 8g and 8h. In contrast, the rainfall textures of $R(Z_H^{ABC})$ in Figs. 8e and 8f are similar to those of $R(K_{DP})$, especially in the rainfall center area. In addition, 99 328 and 99 826 point-wise samples [$R(Z_H)$ versus $R(K_{DP})$] within the PBB-affected area in Fig. 8 were selected and used for detailed comparison for the first and second events, respectively. The scattergrams of the rainfall estimates for the selected samples during these two events are shown in Fig. 11. As shown in Fig. 11a, there are only 42 539 (42.8%) samples [$R(Z_H^M)$ versus $R(K_{DP})$] between the upper and lower diagonal lines during event 1. Similarly, there are only 46 321 (46.4%) samples between the upper and lower diagonal lines during event 2 (see Fig. 11c). Most of these samples correspond to the light-rain regions (i.e., 3-h rainfall less than 20 mm). After attenuation

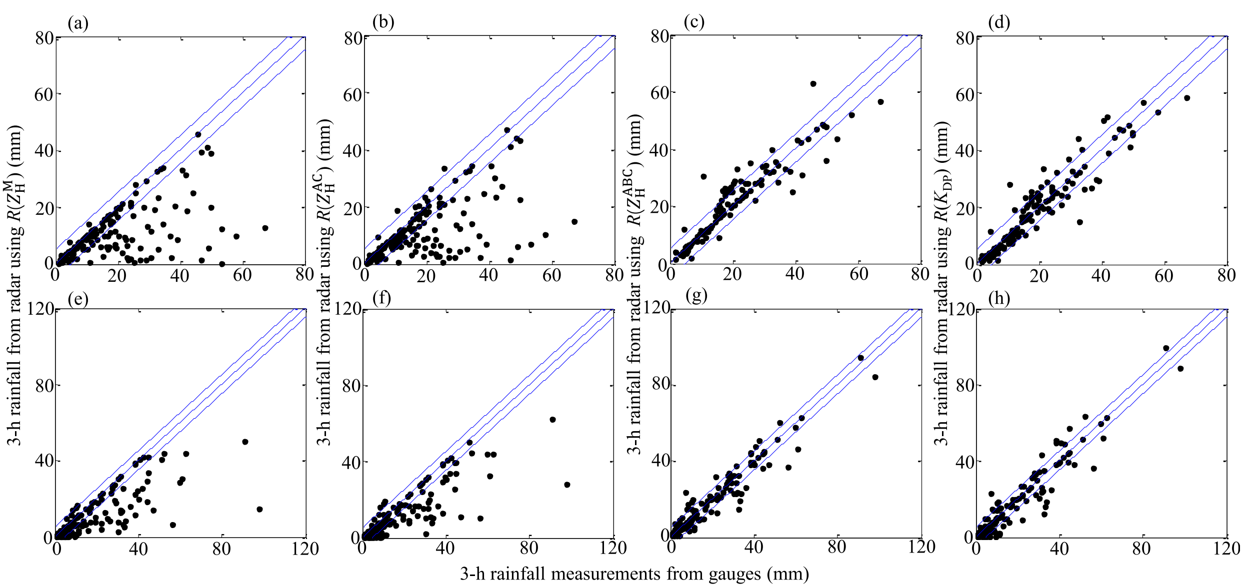

FIG. 10. Scattergrams of the 3-h rainfall estimates from the radar vs the gauge measurements in the PBB-affected areas: (a),(e) derived from $R(Z_H^M)$; (b),(f) derived from $R(Z_H^{AC})$; (c),(g) derived from Z_H^{ABC}; (d),(h) derived from $R(K_{DP})$. (top) Estimates at 1000 UTC 25 May 2019 and (bottom) estimates at 2100 UTC 20 Jun 2019. The three blue lines indicate $y = x$ and $y = x \pm 5$.

TABLE 1. Evaluation results of the 3-h rainfall estimates using different radar rainfall relationships.

Time frame	Radar QPE estimators	Statistical scores			
		E_{BIAS}	E_{NM}	E_{RMS}	E_{CC}
1000 UTC 25 May 2019	$R(Z_H^M)$	0.59	68.52	13.83	0.54
	$R(Z_H^{AC})$	0.63	63.22	13.05	0.57
	$R(Z_H^{ABC})$	1.05	17.27	5.67	0.91
	$R(K_{DP})$	0.95	22.25	6.94	0.87
2100 UTC 20 Jun 2019	$R(Z_H^M)$	0.63	62.26	12.5	0.79
	$R(Z_H^{AC})$	0.68	51.29	10.75	0.85
	$R(Z_H^{ABC})$	0.98	16.54	4.75	0.96
	$R(K_{DP})$	0.97	21.45	5.71	0.95

correction, the total number of samples lying between the upper and lower diagonal lines increased to 49 684 (50%) and 51 609 (51.7%), respectively, for the two events (see Figs. 11b,e).

Although some of the moderate rainfall estimates (i.e., higher than 20 mm) in the PBB-affected area were enhanced, the underestimation of $R(Z_H^{AC})$ remains a problem. In contrast, there are 89 615 (90.2%) and 79 413 (79.5%) samples between the upper and lower diagonal lines in Figs. 11c and 11f, respectively, which shows excellent agreement between $R(Z_H^{ABC})$ and $R(K_{DP})$. The improvement brought by $R(Z_H^{ABC})$ compared to $R(Z_H^M)$ or $R(Z_H^{AC})$ is dramatic, especially in the heavy-rain regions where the 3-h rainfall estimates are higher than 50 mm. Such dramatic improvement is mainly attributed to the implementation of the PBB correction.

In addition, extra attention was paid to the higher rainfall estimates of $R(Z_H^{ABC})$ compared to $R(K_{DP})$. As shown in Fig. 11c where the radar rainfall estimates are less than 20 mm, these samples are mainly from the range gates featuring $\rho_{HV} < 0.85$, $Z_H > 20$ dBZ, but $K_{DP} > 1°$ km^{-1}. These range gates were suspected to be contaminated by the NUBF effect and many of them were eliminated during K_{DP} estimation. However, the Z_H measurements seem to be less affected by the NUBF effect. The attenuation can be corrected with ever-increasing PIA values along the radial profile, and the PBB correction only requires that the corrected Z_H and K_{DP} are consistent in the range gates with $\rho_{HV} \geq 0.98$ and $\rho_{HV} \leq 1$. As a result, $R(Z_H^{ABC})$ shows some higher rainfall accumulations in the polygonal area in Fig. 8e compared to $R(K_{DP})$ in Fig. 8g. Moreover, the rainfall estimates derived from $R(Z_H^{ABC})$ are weaker than those derived from $R(K_{DP})$, particularly when rainfall estimates are higher than 20 mm in Fig. 11f. Combining the scores of $R(K_{DP})$ in Table 1, $R(Z_H^{ABC})$ seems more reasonable than $R(K_{DP})$ for rainfall estimation.

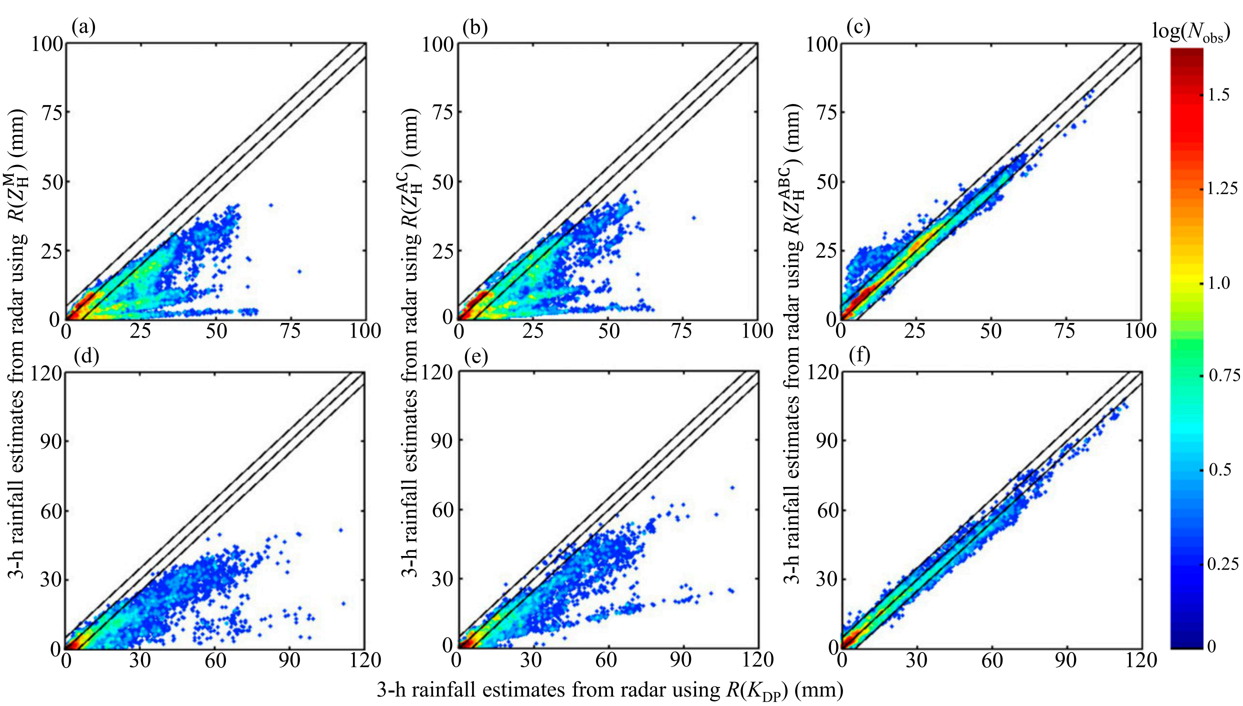

FIG. 11. Scattergrams of the 3-h rainfall estimates based on $R(Z_H)$ vs $R(K_{DP})$ in the PBB-affected areas: (a),(d) $R(Z_H^M)$ vs $R(K_{DP})$; (b),(e) $R(Z_H^{AC})$ vs $R(K_{DP})$; (c),(f) $R(Z_H^{ABC})$ vs $R(K_{DP})$. (top) Estimates at 1000 UTC 25 May 2019 and (bottom) estimates at 2100 UTC 20 Jun 2019. The three black lines indicate $y = x$ and $y = x \pm 5$.

At the very least, the combination of more K_{DP}–R relationships may be necessary to enhance the performance of $R(K_{DP})$.

d. Discussion

Although significant progress has been made in PBB correction, a number of relevant issues may need to be considered in practical implementations:

(i) PBB is not the only quality control issue in polarimetric radar applications. The residual ground clutter contaminations on Z_H, ρ_{HV}, and Ψ_{DP} measurements are not significant for the CPOL radar due to its high altitudes and the rigorous application of the CMD algorithm. However, clutter contaminations may still be a critical issue for many low-altitude S-band radars. More complex signal filtering and processing techniques may be therefore required, along with the PBB correction scheme.

(ii) The 0° elevation angle radar data during warm season precipitation events were used in this paper, which could partially explain the high accuracy of the precipitation estimates relative to the gauge rainfall reports. However, the bright band effect may be a more serious issue during cooler seasons or shallow stratiform events. In such cases, multiradar observations, including vertical profiles of reflectivity, are necessary to fully resolve the precipitation structures and to provide reliable QPE.

(iii) Although the radar measurements and QPE products were significantly improved after PBB correction, the correction scheme was established based on a fixed K_{DP}–Z_H relationship that may cause some uncertainties. On the one hand, the K_{DP}–Z_H relationship may be somewhat different in different precipitation events. Ideally, it should be adjusted according to different precipitation microphysics. On the other hand, the K_{DP} at X band/S band are more/less sensitive to rain than that at C band. When extending this PBB correction method for S- and/or X-band applications, the K_{DP}–Z_H relationship should be reestablished. Fortunately, construction of local K_{DP}–Z_H relationships at different frequencies should not be difficult nowadays.

(iv) The residual δ and NUBF effects along the radial profiles of Φ_{DP} may contaminate the K_{DP} estimation, which will result in the overestimation of $Z_H^B(r_b)$ and, subsequently, degrade the PBB correction performance. This phenomenon is closely related to the mixed-phase hydrometeors or the edge area of rainstorms, which should be carefully treated during practical implementations.

(v) This paper performed attenuation correction first and then PBB correction afterward. Although not presented, if PBB correction is conducted first and attenuation correction is incorporated afterward, similar results can be obtained. The key is that both A_H and K_{DP} are immune to attenuation and PBB effects.

5. Summary

PBB correction is an important step in weather radar data quality control, and it is critical for rainfall estimation and subsequent flood warnings, especially in complex urban and mountain environments. This paper developed an improved PBB correction approach for polarimetric radar applications. The practical performance of this PBB correction technique was verified by comparing the spatial continuity of reflectivity, the consistency between radar-measured and DSD-derived K_{DP} versus Z_H, as well as radar-derived QPE. The main findings are summarized as follows:

(i) The spatial continuity of reflectivity can be effectively enhanced after attenuation and PBB corrections, and the reflectivity measurements of the CPOL radar in PBB-affected areas can become more consistent with the collocated S-band radar measurements. This is particularly evident in the rainstorm center area, where the Z_H measurements are larger than 30 dBZ. The PBB correction contributes more to mitigating the Z_H bias than the attenuation correction along the PBB-affected radial profiles.

(ii) The consistency between radar-measured K_{DP} and Z_H can be incrementally enhanced after attenuation and PBB corrections. While attenuation correction can partly mitigate some biases in radar-measured K_{DP} and Z_H, PBB correction can further enhance the measurement quality. The radar-measured K_{DP} and Z_H are more consistent with DSD-derived K_{DP}–Z_H distributions after PBB correction.

(iii) Rainfall estimates based on the Z_H measurements in PBB-affected areas can be significantly improved and the spatial continuity of the derived rainfall field is more realistic after PBB correction. The $R(Z_H)$ tends to be more comparable with $R(K_{DP})$ after attenuation and PBB corrections.

The PBB correction procedure developed in this paper is not limited to C-band applications. It is very flexible and can easily be extended to S- and/or X-band radar frequencies. With this improved PBB correction approach, it is also expected that multi-radar-based composite reflectivity will be more complete, especially at the lower atmospheric layers over complex terrain regions. The enhanced reflectivity is useful for many relevant applications such as QPE, hydrometeor identification, nowcast of severe rainfall and flood, and the development of data assimilation techniques to improve numerical weather prediction models.

Acknowledgments. This research was primarily supported by the National Natural Science Foundation of China (NSFC) under Grant 41705018 and the Zhejiang Provincial Natural Science Fund through award LY17D050001. The C-band polarimetric radar, disdrometer and gauge data were provided by Hangzhou Meteorological Bureau (HMB). The authors thank the forecasters at HMB for the discussion of severe weather events included in this study.

REFERENCES

Bech, J., B. Codina, J. Lorente, and D. Bebbington, 2003: The sensitivity of single polarization weather radar beam blockage correction to variability in the vertical refractivity gradient. *J. Atmos. Oceanic Technol.*, **20**, 845–855, https://doi.org/10.1175/1520-0426(2003)020<0845:TSOSPW>2.0.CO;2.

Brandes, E. A., G. Zhang, and J. Vivekanandan, 2002: Experiments in rainfall estimation with a polarimetric radar in a subtropical environment. *J. Appl. Meteor.*, **41**, 674–685, https://doi.org/10.1175/1520-0450(2002)041<0674:EIREWA>2.0.CO;2.

Bringi, V. N., T. D. Keenan, and V. Chandrasekar, 2001: Correcting C-band radar reflectivity and differential reflectivity data for rain attenuation: A self-consistent method with constraints. *IEEE Trans. Geosci. Remote Sens.*, **39**, 1906–1915, https://doi.org/10.1109/36.951081.

Carey, L. D., R. Cifelli, W. A. Petersen, and S. A. Rutledge, 2000: Preliminary report on TRMM-LBA rainfall estimation using the S-Pol radar. Dept. of Atmospheric Science Paper 697, Colorado State University, 21 pp., http://hdl.handle.net/10217/26814.

Chen, H., R. Cifelli, and A. White, 2020: Improving operational radar rainfall estimates using profiler observations over complex terrain in Northern California. *IEEE Trans. Geosci. Remote Sens.*, **58**, 1821–1832, https://doi.org/10.1109/TGRS.2019.2949214.

Diederich, M., A. Ryzhkov, C. Simmer, P. Zhang, and S. Trömel, 2015: Use of specific attenuation for rainfall measurement at X-band radar wavelengths. Part I: Radar calibration and partial beam blockage estimation. *J. Hydrometeor.*, **16**, 487–502, https://doi.org/10.1175/JHM-D-14-0066.1.

Giangrande, S. E., and A. V. Ryzhkov, 2005: Calibration of dual-polarization radar in the presence of partial beam blockage. *J. Atmos. Oceanic Technol.*, **22**, 1156–1166, https://doi.org/10.1175/JTECH1766.1.

Gou, Y., H. Chen, and J. Zheng, 2019: An improved self-consistent approach to attenuation correction for C-band polarimetric radar measurements and its impact on quantitative precipitation estimation. *Atmos. Res.*, **226**, 32–48, https://doi.org/10.1016/j.atmosres.2019.03.006.

Hubbert, J., and V. N. Bringi, 1995: An iterative filtering technique for the analysis of copolar differential phase and dual-frequency radar measurements. *J. Atmos. Oceanic Technol.*, **12**, 643–648, https://doi.org/10.1175/1520-0426(1995)012<0643:AIFTFT>2.0.CO;2.

——, M. Dixon, and S. Ellis, 2009: Weather radar ground clutter. Part II: Real-time identification and filtering. *J. Atmos. Oceanic Technol.*, **26**, 1181–1197, https://doi.org/10.1175/2009JTECHA1160.1.

Lang, T. J., S. W. Nesbitt, and L. D. Carey, 2009: On the correction of partial beam blockage in polarimetric radar data. *J. Atmos. Oceanic Technol.*, **26**, 943–957, https://doi.org/10.1175/2008JTECHA1133.1.

Ryzhkov, A., M. Diederich, P. Zhang, and C. Simmer, 2014: Potential utilization of specific attenuation for rainfall estimation, mitigation of partial beam blockage, and radar networking. *J. Atmos. Oceanic Technol.*, **31**, 599–619, https://doi.org/10.1175/JTECH-D-13-00038.1.

Testud, J., E. Le Bouar, E. Obligis, and M. Ali-Mehenni, 2000: The rain profiling algorithm applied to polarimetric weather radar. *J. Atmos. Oceanic Technol.*, **17**, 332–356, https://doi.org/10.1175/1520-0426(2000)017<0332:TRPAAT>2.0.CO;2.

Wang, Y., and V. Chandrasekar, 2009: Algorithm for estimation of the specific differential phase. *J. Atmos. Oceanic Technol.*, **26**, 2565–2578, https://doi.org/10.1175/2009JTECHA1358.1.

Waterman, P. C., 1965: Matrix formulation of electromagnetic scattering. *Proc. IEEE*, **53**, 805–812, https://doi.org/10.1109/PROC.1965.4058.

Zhang, P., D. Zrnić, and A. Ryzhkov, 2013: Partial beam blockage correction using polarimetric radar measurements. *J. Atmos. Oceanic Technol.*, **30**, 861–872, https://doi.org/10.1175/JTECH-D-12-00075.1.